Combustion Mode and Mixing Characteristics of a Reacting Jet in Crossflow

Zehua Zhang[1], Abouelmagd Abdelsamie[2], Cheng Chi[2], Dominique Thévenin[2], Kai H. Luo[3,*]

[1] Center for Combustion Energy, Department of Energy and Power Engineering, Key Laboratory for Thermal Science and Power Engineering of Ministry of Education, Tsinghua University, Haidian District, Beijing, 100084, China

[2] Laboratory of Fluid Dynamics and Technical Flows, University of Magdeburg "Otto von Guericke", Universitätsplatz 2, Magdeburg, 39106, Germany

[3] Department of Mechanical Engineering, University College London, Torrington Place, London WC1E 7JE, United Kingdom

*Corresponding author: K. H. Luo

Email: K.Luo@ucl.ac.uk

Abstract: Understanding of flame anchoring in a jet in crossflow (JICF) configuration is vital to the design of fuel injectors in combustion devices. The present study numerically investigates a

hydrogen rich jet injecting perpendicularly into hot vitiated crossflow using direct numerical simulation (DNS). The governing equations of low-Mach-number multicomponent reactive flows are solved, with a chemical mechanism for hydrogen-air flames containing 13 species and 35 reactions. The mixture-averaged multispecies transport model is employed to calculate the diffusion terms. Development of the reacting flow field and flame shape along the jet trajectory is depicted. The flame is found to be anchored around the jet exit and downstream only on the windward side. The heat release rate and chemical explosive mode analysis (CEMA) are used to identify combustion modes. Distinct from flames stabilized in non-vitiated crossflow, diffusion flame is dominant under the current conditions, though some premixed or partially premixed regions are found on the leeward side of the jet due to turbulent mixing. The near-field mixing of the reacting JICF is quantified by spatial unmixedness, in both 2D and 3D space.

1 Introduction

Jet in cross flow (JICF), also referred to as transverse jet, is a configuration where a jet is injected perpendicularly into a crossflowing fluid and interacts with it [1, 2]. JICF is common in both industrial devices and the natural world. For industrial applications, selected examples are film cooling on turbine blades, fuel injectors in combustors, and air/fuel injection in staged combustors. A fascinating example of JICF in nature is the jet plume from a volcano transported by the crosswind. Due to its broad applicability, the JICF configuration has been studied as a topic of significant technological interest over the past few decades. According to whether there is a chemical reaction

during the subsequent process, a jet in crossflow can be categorized into non-reacting JICF and reacting JICF.

Many early researches on reacting JICF focus on developing empirical formula of the jet trajectory [3, 4]. Later on, flame structure, flame stabilization and emissions under different conditions attract more attention. For instance, Weinzierl et al. [5] used the LES method together with a NO_x model to simulate a reacting JICF and predicted the NO_x emission from an axial-staged combustion system. Pinchak et al. [6] experimentally investigated the effects of jet equivalence ratio, momentum flux ratio and jet geometry on the stability characteristics of a premixed ethylene-air jet injected into a vitiated crossflow. It is reported that at their experiment conditions the flame stabilization process was controlled by flame propagation rather than by autoignition. Wagner et al. [7] also studied the flame stabilization behavior of a premixed ethylene-air jet injected transversely into a vitiated crossflow of lean combustion products. In their experiments, it was observed that the windward flame branch was unsteady and showed both attached and lifted flame behaviors, and chemiluminescence images of the lifted flame showed that both propagation and auto-ignition contributed to flame anchoring.

Among numerous studies of reacting JICF, we refer here to some of those conducted by the direct numerical simulation (DNS) method. DNS uniquely provides fine-scale information regarding instantaneous reacting flow fields and flame structures. Grout et al. [8] reported a three-dimensional DNS of a nitrogen-diluted hydrogen transverse jet injecting into a crossflow of heated air. Results

indicated that the flame stabilized in a low-velocity region only on the jet lee side. Lyra et al. [9] reported a DNS study of reacting JICF together with an experiment, where a hydrogen rich jet injected transversely into a turbulent vitiated crossflow of lean methane combustion products. Different from the previous simulations conducted by the same code [8], the flame structure of non-premixed fuel jet into vitiated crossflow was uniformly stabilized near to the jet exit around its entire circumference. Abdilghanie et al. reported a 3D DNS of a nitrogen-diluted hydrogen jet injecting into a cross-flowing turbulent stream of preheated air, and observed that ignition occurred initially at isolated spots downstream from the jet, and later on a burning flame formed near the jet nozzle[10]. Such a reacting JICF configuration is highly interesting, as a large number of factors like the level of dilution would affect the transient behaviors of ignition and reactions. As shown by the experimental and numerical studies mentioned above, the flame position in a reacting JICF configuration is determined by different types of stabilization mechanisms. A JICF flame can be very complicated and consists of premixed, partially premixed and diffusion flames. Thus, it is necessary to identify the combustion mode of the reacting JICF.

Besides the combustion mode and flame stabilization analysis, another perspective of reacting JICF is emphasized in this paper, which is the goodness of mixing in the flow field. Leong et al. [11, 12] and Demayo et al. [13] conducted a series of experiments in order to quantify the spatial mixing of an air jet in a rich, reacting crossflow. Data of jet mixture fraction based on different passive scalars were used to evaluate planar spatial unmixedness. Results showed that planar spatial unmixedness

decreased rapidly along the jet direction, as expected. A drawback of the previous work is that it only gave information of a plane as a whole, so that detailed information within the plane was all missing. With the advantage of more data points, this study provides spatial mixing information not only within planes but also in three-dimensional space.

In a series of DNS studies [8-10, 14-16], the Navier-Stokes equations were solved in their compressible formulation. Since in most cases, a reacting JICF takes place at low Mach numbers, Ma<<1, a large speedup can be obtained by using a low-Mach number solver compared to a fully compressible one [17]. In the present study, three-dimensional DNS of reacting JICF is conducted using a low-Mach number solver [18]. The jet and crossflow conditions are set similar to [9] so that the results can be qualitatively compared between the two methods. Furthermore, DNS data of reacting JICF are still rare, so the present study also enriches the database of reacting JICF and can serve as benchmark data for LES and RANS models.

2 Numerical setup

2.1 Description of the physical problem

The jet composition is 70% H_2 and 30% He by volume and the crossflow is comprised of combustion products of a lean methane flame (equivalence ratio of $\Phi = 0.46$). The temperature of the jet and crossflow are 407 K and 1640 K, respectively. Two jets at different speeds are simulated, the corresponding parameters are listed in Table 1. Comparing the two cases, the velocity of the crossflow is the same, the difference is the velocity of the jet, and the resulting jet-to-crossflow

momentum flux ratio defined as $J = \rho_j v_j^2 / \rho_c v_c^2$ and the jet Reynolds number based on jet velocity and jet diameter. ρ is density and v is velocity, the subscripts j and c refer to jet and crossflow respectively.

Table 1. Physical parameters for the two simulated jets.

	Jet velocity v_j(m/s)	Crossflow velocity v_c(m/s)	Momentum flux ratio	Jet Reynolds number
Case 1	291	59	9	2420
Case 2	85	59	0.8	707

2.2 Algorithm

The governing equations of low-Mach-number multicomponent reactive flows are solved. A brief summary of the equations are listed below. The derivation from the compressible formulations to low-Mach-number formulations can be found in refs. [19,20].

In the case of low-Mach-number flows the pressure p is separated into a thermodynamic part $p_0(t)$ which is spatially uniform and a hydrodynamic part $\tilde{p}(x,t)$, $\tilde{p}(x,t) \ll p_0(t)$. The conservations equations can be summarized as follow:

$$p = \tilde{p}(x,t) + p_0(t) \tag{2.1}$$

$$\frac{\partial \rho}{\partial t} + \boldsymbol{\nabla} \cdot (\rho \boldsymbol{v}) = 0 \tag{2.2}$$

$$\frac{\partial \rho Y_k}{\partial t} + \boldsymbol{\nabla} \cdot (\rho \boldsymbol{v} Y_k) + \boldsymbol{\nabla} \cdot \boldsymbol{F}_k = M_k \omega_k \quad (k = 1, \dots, N_s) \tag{2.3}$$

$$\frac{\partial \rho \boldsymbol{v}}{\partial t} + \boldsymbol{\nabla} \cdot (\rho \boldsymbol{v} \otimes \boldsymbol{v}) + \boldsymbol{\nabla} \cdot \tau = -\boldsymbol{\nabla} \tilde{p} \tag{2.4}$$

$$\frac{\partial \rho e_t}{\partial t} + \boldsymbol{\nabla} \cdot (\rho \boldsymbol{v} e_t) + \boldsymbol{\nabla} \cdot \boldsymbol{Q} = 0 \qquad (2.5)$$

$$p_0 = \frac{\rho R_0 T}{M} \qquad (2.6)$$

$$e_t = \frac{1}{2}(\boldsymbol{v} \cdot \boldsymbol{v}) + h - \frac{p}{\rho} \qquad (2.7)$$

$$\boldsymbol{Q} = -\lambda \, \boldsymbol{\nabla} T + \sum_{k=1}^{N_s} (h_k \boldsymbol{F}_k) \qquad (2.8)$$

$$\tau = \frac{2}{3}\mu(\boldsymbol{\nabla} \cdot \boldsymbol{v})\boldsymbol{I} - \mu(\boldsymbol{\nabla} v + (\boldsymbol{\nabla} v)^t) \qquad (2.9)$$

where, ρ represents the density, $\boldsymbol{v}$ the velocity vector, Y_k the mass fraction of species k, $\boldsymbol{F}_k$ the species diffusion flux, M_k the molar mass of species k, ω_k the molar production rate, N_s the total number of species in the flow, p the pressure, τ the viscous strain tensor, e_t the specific total energy, $\boldsymbol{Q}$ the heat flux, λ the thermal conductivity, h_k the specific enthalpy of species k, R_0 the perfect gas constant, T the temperature, M the mixture molar mass, h the mixture specific enthalpy, $\boldsymbol{I}$ the unit tensor and μ the dynamic viscosity, ^{t} the transposition.

The low-Mach Navier-Stokes system coupled with detailed physicochemical models is solved with an in-house code named DINO, which is a high-order finite-difference code for low-Mach reactive flows, and has been used and validated in a variety of applications, e.g. [18,21,22]. A sixth-order centered explicit finite difference scheme is used to compute the spatial derivatives. An explicit fourth-order Runge-Kutta time integrator is employed for temporal integration. Chemical reactions, physical properties and transport properties are computed by Cantera [23]. The mechanism

of Li et al. [24], which consists of 13 species and 35 reactions, is used to represent the hydrogen-air

chemical kinetics. As the multicomponent diffusion may be numerically expensive in the current

3D simulation [25], the mixture-averaged model [26] (also called Hirschfelder-Curtiss approximation) is

used. The thermo-diffusion effect [20] (also called Soret effect) plays a noticeable role in hydrogen

combustion systems and is taken into account in the present study.

2.3 Computational domain and boundary conditions
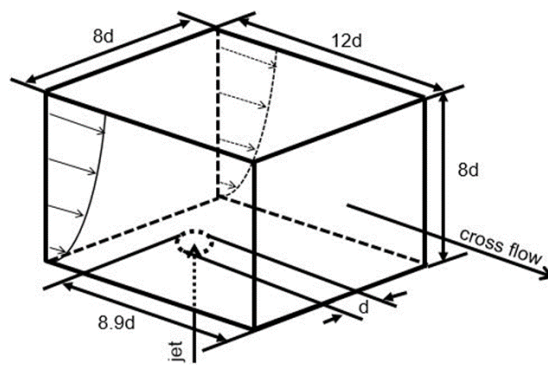
Figure 1. Schematic diagram of the three-dimensional (3D) simulation domain, where d is the jet

diameter.

DNS is conducted to study a round jet injecting into a turbulent crossflow. The computational

domain is shown in Fig. 1, where the domain length in streamwise, spanwise and wall-normal

directions is 12d, 8d, and 8d, respectively, with $d = 1.5 \times 10^{-3}$m the corresponding jet diameter.

The computational domain is chosen to be large enough to avoid direct interactions between the jet

and the boundaries. In the meantime, the domain is made smaller than that in the experiments [9] and

in the DNS of Lyra et al. [9] to reduce computational costs. The qualitative effects of such a choice on

the subsequent simulation results would be negligible, although the jet trajectories are slightly modified. A uniform grid comprised of $900 \times 600 \times 600$ points is used. A maximum spatial resolution of $20 \, \mu$m is reached to ensure that there are sufficient near-wall grid points to resolve the boundary layer. To estimate the y^+ distance, the following parameters are used; the freestream velocity $v_c = 59$ m/s, average density $\rho_{ave} = 1.88 \times 10^{-1}$ kg/m^3, dynamic viscosity $\mu = 5.75 \times 10^{-5}$ kg/ms, the boundary layer length scale is set to be the jet diameter[29] which is $d_j = 1.5 \times 10^{-3}$m. It turns out that the first point of the current mesh locates at y^+=0.5 and there are 20 points below y^+=10. Turbulent fluctuations are superimposed on the mean velocity field of a fully developed channel flow to initialize a turbulent channel flow. During the simulation this pre-calculated turbulent velocity field is used as the inflow boundary condition. In the streamwise direction, the turbulent flow enters the domain from an inflow boundary and exits the domain from an outlet boundary where the pressure is kept constant. In the spanwise direction, periodic boundary conditions are applied. On the top, a symmetry boundary condition is used. At the lower border, a mixed boundary condition is used (inflow boundary at the jet inlet and wall otherwise). For the jet inlet area, the velocity is prescribed in the wall-normal direction. The jet is assumed as a laminar flow. For areas other than the jet inlet, the boundary is assumed as no-slip adiabatic wall, velocity on the wall is therefore zero. A hyperbolic tangent function is used to smooth the profile between the isothermal wall boundary and jet inlet boundary. Simulation is pursued for at least 2τ to ensure

the simulation has reached a statistically steady condition, where the flow-through time $\tau = 0.3$ ms

is defined as the streamwise length divided by the mean crossflow velocity.

3 Results and discussion

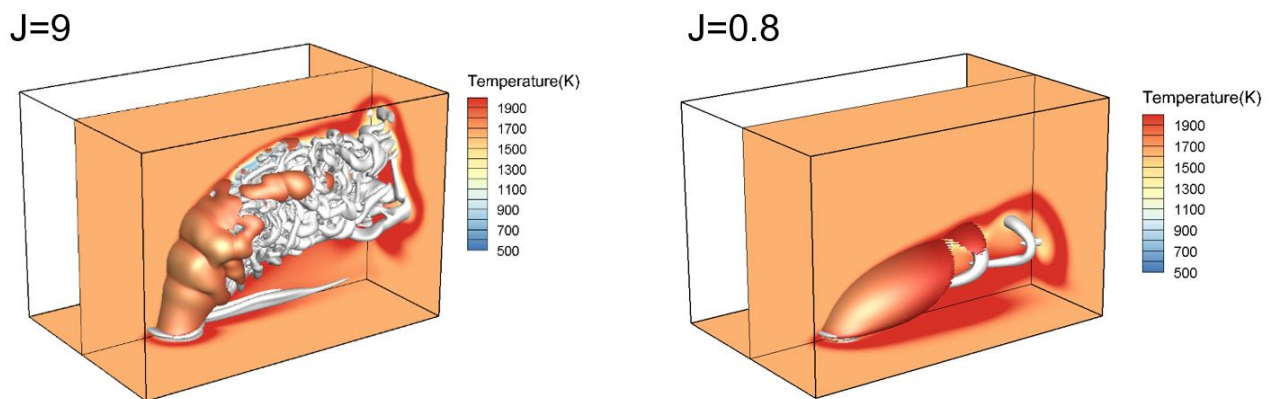### 3.1 Mean and instantaneous reacting flow fields

Figure 2. Instantaneous snapshots of 3D reacting jet in crossflow at $t = 2\tau$. The jet is visualized

by the isosurface of heat release rate, $HRR = 0.99HRR_{max}$, colored by temperature. The flow

vortex structure is visualized using the Q-criterion (gray), $Q = 2 \times 10^8$ s^{-2} for $J = 9$ and $Q =$

5×10^8 s^{-2} for $J = 0.8$. Temperature contours are shown on the 2D slices.

The overall structure of the jet flames is shown in Fig.2. For both cases, areas with the highest

heat release rate are concentrated on the windward side of the jet. The flame front is wrapped

around the jet outlet. The vortex structure is visualized by the Q-criterion, as is shown by gray

surface in Fig. 2. For both cases, the near field coherent structure locates behind the reaction zone,

and turbulence is visually much stronger in case 1. Here "coherent" means persistent flow patterns with a lifetime and spatial extent larger than the turbulence integral scale[27]. However, it must be kept in mind that using the Q-criterion to show the vortex structure can be somewhat arbitrary, since the specific value of the Q-criterion changes the perception of the nature and the size of the flow structure[28]. In order to make a fair comparison, a non-dimensionalized Q-criterion is used, with scaling velocity being the jet velocity and scaling length being the jet diameter[29]. The comparison is shown in Fig. 3. The windward and leeward structures captured in the two cases show distinct behaviors. Firstly, in Case 1 where $J = 9$, the vortex rings form almost immediately after the injection, while in Case 2 where $J = 0.8$, the vortex rings form later; the first ring structure appears after the jet has been largely bent. Secondly, when $J = 9$, the vortex rings roll up and distort as they interact with the crossflow; a similar behavior has also been observed in experiments by Nair et al.[29]. In contrast, for $J = 0.8$ the vortex rings retain their shape and gradually decay with the flow. In the following analysis, the more interesting Case 1 is retained for a detailed investigation.
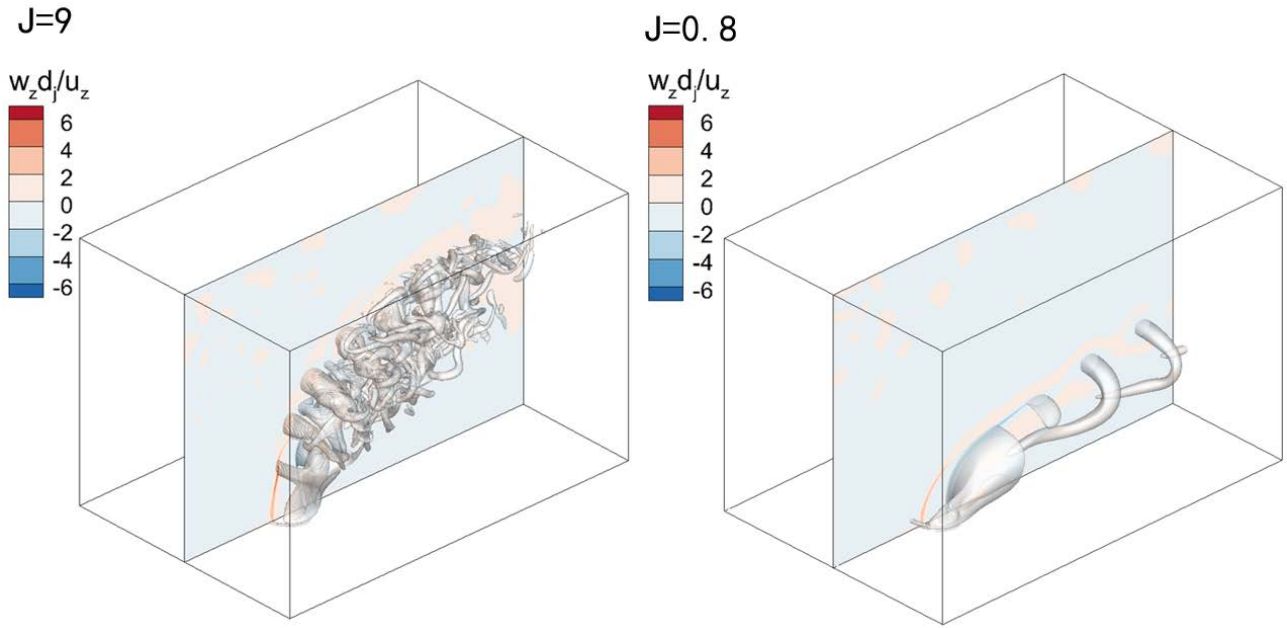
Figure 3. Instantaneous 3D visualization of normalized Q-criterion iso-structures constructed at $Q\,d^2/u_j^2 = 0.2$, where d is the jet diameter and u_j is the jet velocity. Colors in the midplane and on the isosurfaces show normalized vorticity in spanwise direction, $w_z\,d/u_j$.

Typical vortex structures of jet in crossflow are tagged in Fig. 4, including jet shear layer ① on the windward side, horseshoe vortices ② near the lower boundary, and counter-rotating vortex pairs ③ downstream. The shear layer vortex grows larger and wider as the height increases, and then breaks into smaller vortex structures. This trend is marked with the marker ①a to ①d, in Fig. 4a, Fig. 4b and Fig. 4d. The marker ② indicates two legs of a horseshoe vortex (or necklace vortex). The horseshoe vortex is formed upstream of the jet exit and wrapped around the jet, its presence is shown in Fig. 4a and Fig. 4b, and is more visible in Fig. 2. The marker ③ indicates the

contour-rotating vortex pair (CVP), which is the main vortical feature in JICF and dominates the flow structure downstream of the jet. Wake vortices, another vortical feature on the lee side of the jet, are not observed in Fig. 4. It suggests that, in the current case, the interaction between the lee-side jet shear layer and the wall is too weak to generate any wake vortices.
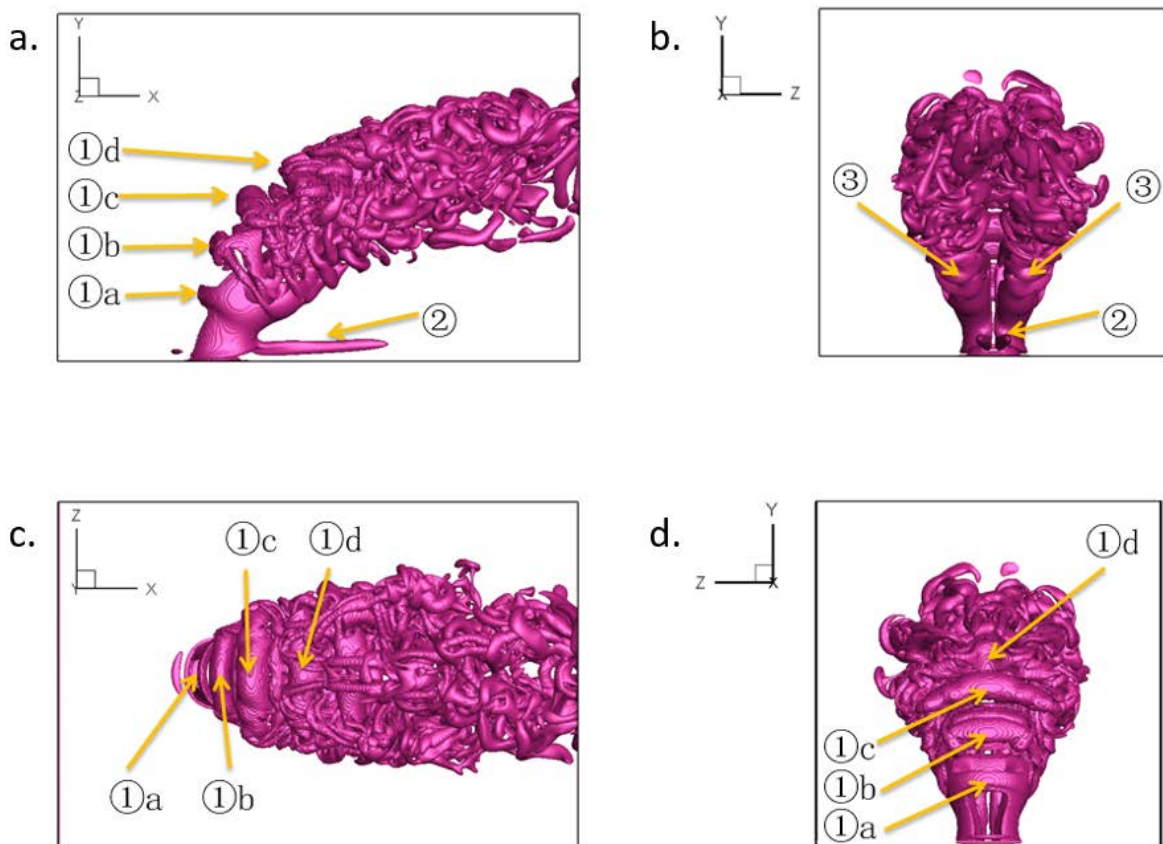

Figure 4. The isosurfaces of the Q-criterion applied to the instantaneous flow field at $t = 2\tau$. The Q-criterion value, $Q = 2 \times 10^8 \text{s}^{-2}$ is selected so that the isosurface is neither too dense nor too sparse.

JICF flow fields are characterized by a jet injection transverse to the crossflow direction. After ejecting from the exit, the jet is deflected and curves in the direction of crossflow, as shown by the jet trajectory (black line) in Fig. 5. There are many different ways to define a jet trajectory, and here the jet trajectory is defined as the stream line starting from the center of the jet exit.

In order to demonstrate how flow field and flame structure develop along the jet trajectory, properties on five different slices are plotted in Fig. 6. These slices are placed to be perpendicular to the jet trajectory. The distance between center of jet exit and the intersections of jet trajectory and the slices ranges from $0.2d$ to $6d$ ($0.2d$, $1d$, $2d$, $4d$, $6d$). Locations of the cross sections are shown by dashed white lines in Fig. 5. Near the jet exit ($0.2d$, slice ①), the momentum of the jet did not have enough time to be changed by the impulse of crossflow. The flow field near this area is very much like a flow around a circular cylinder. At a little distance from the entry point, the originally round jet cross section becomes oval, as shown by the velocity contour on the $1d$ slice ②. This can be easily understood if we recall the flow around a circular cylinder, where there are stagnation points and high pressure zones upstream and downstream. Lower pressures on both sides attract the jet to expand at its lateral edges. The shearing between the jet lateral edges and crossflow results in a kidney-shaped jet crosssection; the development of this kidney-shaped jet cross section can be seen from the $1d$ slice to the $4d$ slice (numbers ② to ④). As the jet trajectory further bends, the jet is flanked by shedding vortices, those vortices on both sides then develop into a counter rotating vortex pair (CRVP), as shown by the development of vorticity magnitude in Fig. 6 Evolution of the

CRVP of this reacting JICF is very similar to that of the non-reacting ones[30, 31]. CRVP is the most prominent vortex structures of JICF and is the primary mechanism for fast mixing between the fuel jet and crossflow[2]. The highest temperature is found in the recirculation zones on the jet lee side. If we compare the development of the flame shape and the fuel jet, from slices ① to ④, it can be inferred that an annular (starting with a circular shape, then increasingly deformed further downstream) reaction zone surrounds the fuel-rich jet. This suggests that the combustion is in a diffusion flame mode; this point will be further explained in the next section.
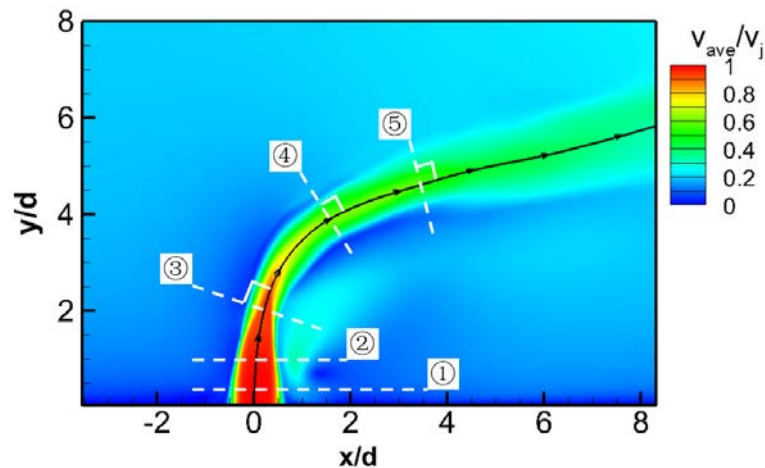
Figure 5. Time-averaged velocity magnitude in the spanwise midplane. The mean flow field has been calculated for every time-step starting from 1.8τ up to 2τ. Jet trajectory is shown by the black line. Positions of cross-sections are shown by dashed white lines. Intersections of cross-sections and jet trajectory locate at a distance of $0.2d$, $1d$, $2d$, $4d$ and $6d$ from the jet exit.
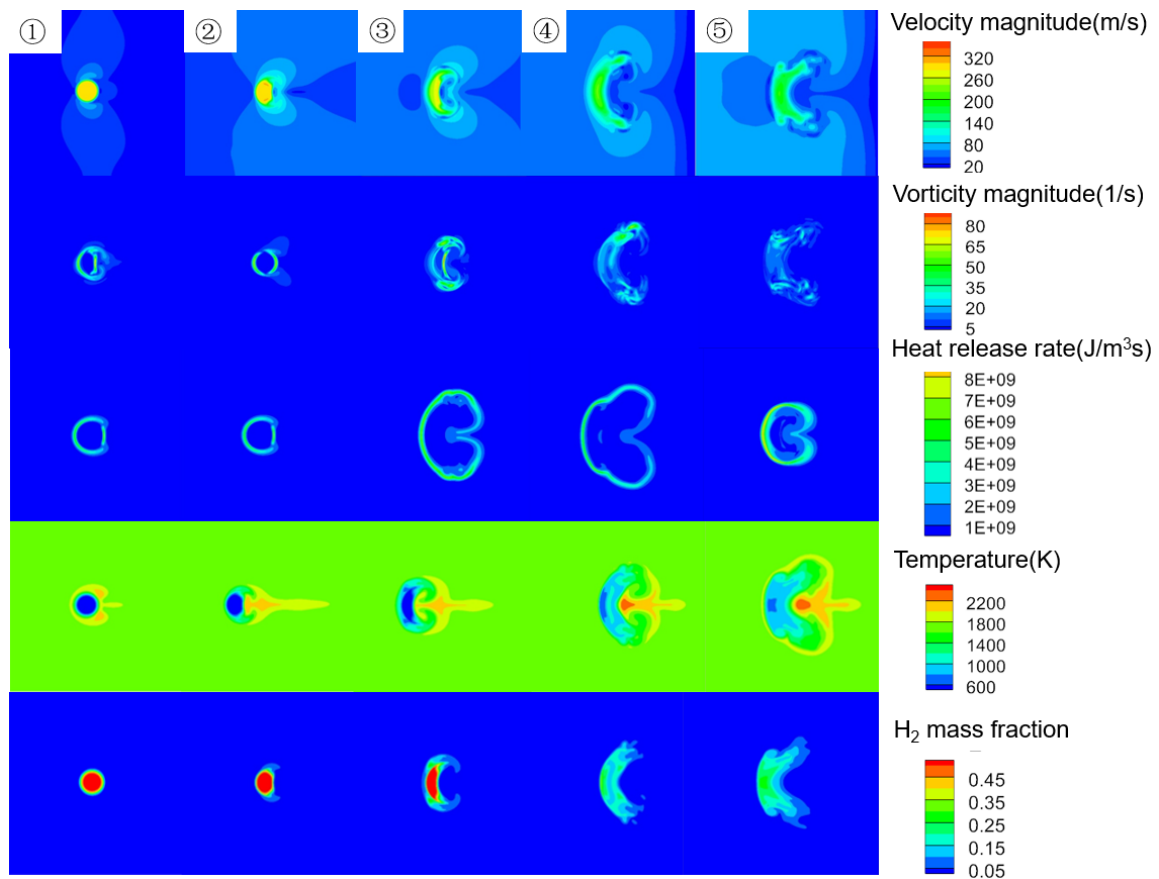
Figure 6. Velocity magnitude, vorticity magnitude, heat release rate, temperature and H_2 mass fraction in different slices. Instantaneous results at $t = 2\tau$.

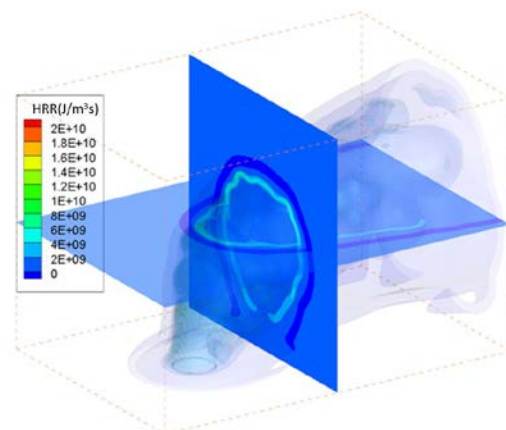## 3.2 Flame stabilization and combustion mode

Figure 7. Volume rendering of the instantaneous heat release rate (HRR).

Lyra et al.[9] used the CEMA method to analyze the combustion mode of the reacting jet, and found that the flame front is characterized by a negative explosive mode. This finding is confirmed in the present study using the CEMA method alone. In order to further examine the nature of the flame, we use the heat release rate together with CEMA[32,33]. The focus of the present analysis is on the burning mode of the local flames, complementing previous studies.

The first step is to locate the position of the flame. Heat release rate (HHR) is the most direct parameter to determine the reaction zone. An instantaneous snapshot of the HHR is shown in Fig. 7. Contours of HHR is used to identify reaction zones. Near the exit, the position of the flame is around the jet, and downstream, combustion takes place on the windward side of the jet.

The second step is to use the heat release rate and CEMA method together. The reaction zone is delineated by a contour line of which the value is 20% of the maximum heat release rate, as shown by the black line in Fig. 8. The CEMA method is based on an evaluation of the largest non-conservative eigenvalues of the chemical Jacobian, and the visualization of the eigenvalues is defined by the following equation,

$$\gamma_e = \text{sign}(\text{Re}(\lambda_e)) \cdot \log_{10}(1 + |\text{Re}(\lambda_e)|)$$

where 'sign' is the sign function and 'Re' denotes the real part of a complex number. λ_e is the largest non-conservative eigenvalue of the chemical Jacobian. It must be kept in mind that the CEMA analysis does not take into account transport. A positive value of γ_e indicates the mixture composition is sufficient to support combustion under adiabatic conditions. A negative value means

the mixture is chemically non-explosive in isolation. Diffusion flames can be identified by peaks of

reaction rates combined with the non-explosive mode [32]. Figure 8 shows that for most of the

reaction zones in both cases, the flame is in diffusion mode. Near the jet exit the flame immediately

forms around the nozzle, suggesting that the reaction happens very close to the exit as fuel mixes

with the crossflow. It is interesting to note that, in Case 1, on the windward side of the jet, explosive

mode mixtures are also found within reaction zones. Zero-crossing of γ_e identifies premixed flame

where chemically explosive reactants burn into non-explosive combustion products. In Case 2,

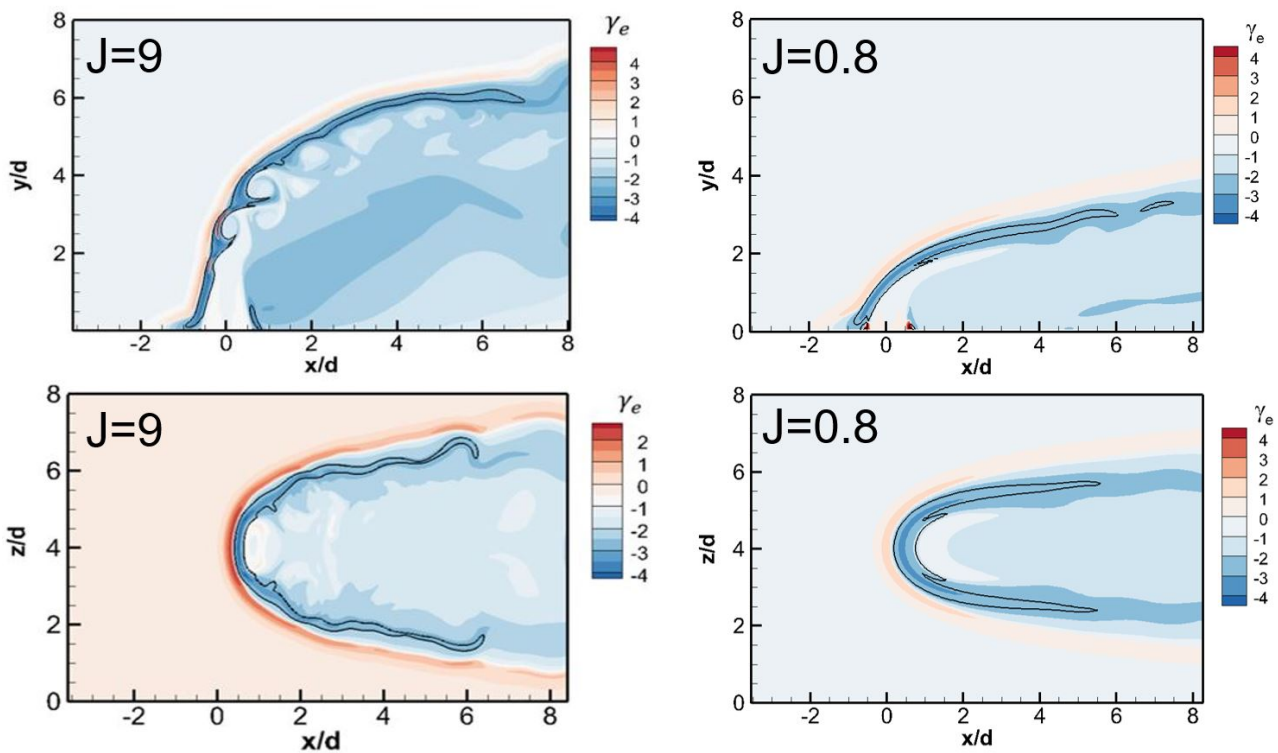however, all reaction zones are identified to be diffusion flames.

Figure 8. Chemical explosive mode (positive values of γ_e) in the spanwise and wall-normal

midplanes. Reaction zone is delineated by black isocontours of heat release rate at a value of 20%

of the maximum.

Efforts are made to investigate the possible causes of the presence of passive eigenvalues in the reaction zone as shown by red regions within blacklines. It is shown in the upper left picture in Fig. 8 as well as in Fig. 9. From the perspective of chemical reactions, eigenvectors used in CEMA and the corresponding components distribution should provide some insights. Here, we focus on the effects of the entrainment of jet/crossflow and the turbulent mixing. The vorticity magnitude near these passive γ_e regions are found to be the highest of the whole domain, so the strong shearing between jet and crossflow could have played an important role. The question is: does the presence of explosive mixtures in the windward region occur due to turbulent mixing or entrainment of fuel and air mixtures?

Entrainment reflects the rate at which fluid is entrapped into the large vortical region from the surrounding irrotational fluid[34]. Mixing, on the other hand, proceeds at smaller scales and is governed by the molecular properties of the fluids, and can be accelerated by strong turbulence/shearing. Here, a passive scalar is used to depict the entrainment regions, and different values of the passive scalar are used to show the possible extent of those regions. As shown in Fig. 9, since the various values of the passive scalar correspond to different entrainment areas, three different values are given. Line 3 depicts a wider entrainment area and line 1 depicts a smaller one. It is observed that the passive γ_e locates on the windward side of the entrainment region. So, the presence of positive γ_e cannot be regarded as a result of entrainment. Based on the analysis above,

what happens on the leading edge of the jet is: the fuel and air mix at a scale smaller than that of the

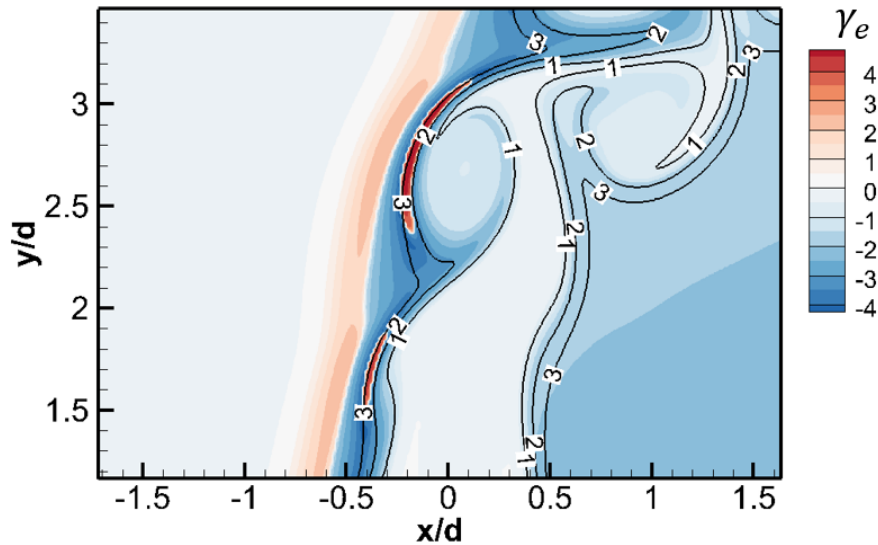jet shear vortex and chemical reaction happens in those fast mixing areas.

Figure 9. Chemical explosive mode (positive values of γ_e) in the wall-normal midplane.

Entrainment is quantified by black isocontours of a passive scalar at three different levels.

3.3 Mixing characteristics

Whether it is for scientific interest or engineering design, researchers have always been very

interested in the mixing process of the jet with the cross flow [1,2,35,36]. In the experiments[11-13], due to

limitations of the measurement methods, the obtained mixedness is usually only based on isolated

data points in a plane. This is not sufficient to get a full picture of the mixing process. This

highlights the advantage coming with abundant data points from numerical simulations. Using the

data of DNS, one can calculate mixedness in the 2D space or even the 3D space, leading to a more

detailed understanding of the mixing progress of the jet and the crossflow. In this section, firstly, the limitations of the traditional method are demonstrated. Secondly, goodness of mixing is studied in 2D and 3D space. Lastly, mixing characteristics of the $J = 9$ case and the $J = 0.8$ case are compared.

3.3.1 Definition of spatial unmixedness.

In order to quantitatively study the mixing process of the reacting JICF, researchers used the parameter called "spatial unmixedness", U_s. Similar concepts can be traced back to 1952, Danckwerts [37] discussed the parameters used to measure the "goodness of mixing" of both liquid-solid and liquid-liquid systems. Later, U_s was modified for specific uses [38]. U_s is derived from the mixture fraction, and because the mass of carbon element is conserved during the reaction, the jet mixture fraction can be defined based on the mass fraction of carbon:

$$f = \frac{Y_{main} - Y_{sample}}{Y_{main} - Y_{jet}}$$

where, Y_{main} and Y_{jet} are the carbon mass fraction in crossflow and jet, respectively. Y_{sample} is carbon mass fraction at any position in space. Then, spatial unmixedness, U_s, is a normalized parameter defined as:

$$U_s = \frac{f_{var}}{f_{ave}(1 - f_{ave})}$$

where, f_{ave} is the average of jet mixture fraction and f_{var} is the variance. U_s reflects the goodness of the mixing of a system; when the system is perfectly mixed, $U_s = 0$, and when the system is totally unmixed, $U_s = 1$.

3.3.2 Spatial unmixedness in 3D space.

By definition, U_s can be used in both two-dimensional and three-dimensional space of any size, as long as there are enough sample points measured within that space. Previous studies only measured planar spatial unmixedness at certain cross sections perpendicular to the cross flow direction. But in this study, abundant data points make it possible to calculate U_s on a smaller scale, thus much more detailed information related to mixing can be revealed. The following analysis is based on data from Case 1 ($J = 9$). Firstly, U_s is calculated in smaller two-dimensional areas to study mixing within a plane. Secondly, U_s is extended to three-dimensional space to demonstrate mixing properties of the reacting jet in crossflow.
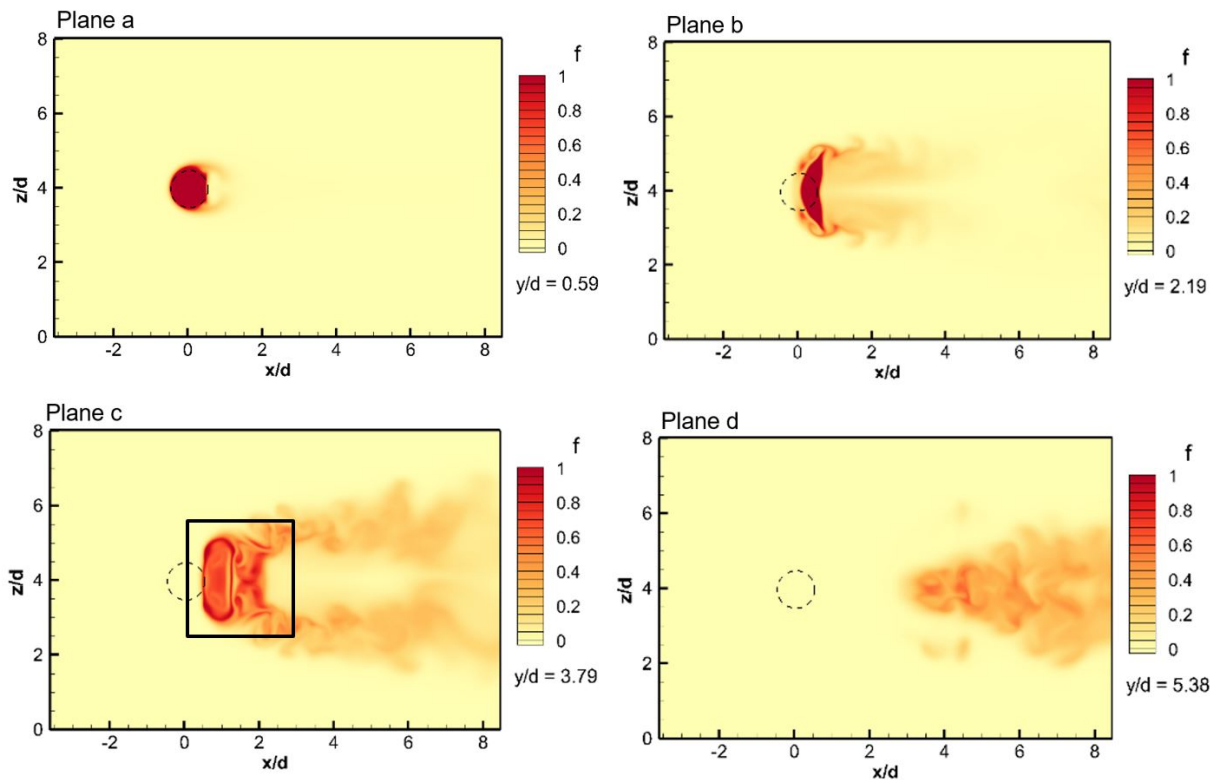
Figure 10. Distribution of the mixture fraction f on planes at different heights. These four planes are named a, b, c and d. The heights of planes are y/d=0.59, 2.19, 3.79 and 5.38. The black dashed line shows position of the jet exit.

Before calculating U_s in smaller 2D areas, the data of several horizontal planes are used to calculate U_s for each plane. Meanwhile, another parameter characterizing mixing goodness, referred to as the scale of segregation, is also calculated. Its purpose is to show the part of the information that U_s cannot express. Figure 10 shows the mixture fractions on cross sections parallel to the bottom surface. Mixing between the jet and the crossflow can be divided into two parts, interminglement and molecular interdiffusion. Interminglement is a mechanical mixing process, through which fluids are broken up into "clumps". Interdiffusion happens across the boundaries of fluid clumps. As shown in Fig. 10, when y/d increases, the shape of the jet clump becomes indeterminate and the boundaries become diffuse. The scale of segregation [37] is a vital quantification of the clumps; it reflects the "average diameter" of the clumps, though it is not easily visualized. The scale of segregation is defined as:

$$R(r) = \frac{\overline{(f_1 - f_{ave})(f_2 - f_{ave})}}{\overline{(f - f_{ave})^2}}$$

$$S = \int_0^\infty R(r)dr$$

where $R(r)$ is the coefficient of correlation between values of mixture fraction f at points separated by a distance r. The linear scale of segregation S is defined as the linear integration of

$R(r)$. Magnitude of S varies in the same sense as the size of "clumps". Results are shown in Fig.

11. As plane positions rise, the length scale of jet mixing first increases and then decreases; the

maximum value of S appears around $y/d = 4$. However the trend of U_s is very different. U_s

first increases and then remains constant, then decreases. Magnitude of U_s reflects the extent to

which the concentration in the jet departs from the mean value of the whole plane. This fact

highlights the necessity of calculating U_s in smaller areas so that detailed mixing characteristics
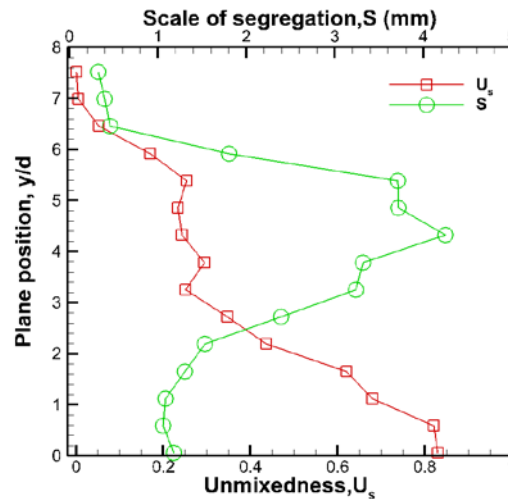
can be obtained.

Figure 11. Scale of segregation S and spatial unmixedness U_s in horizontal cross-sections.

Plane c in Fig. 10 is used as an example. Firstly, the plane is divided into a 180×120 mesh.

The original calculation mesh is 900×600, so each new grid contains 25 data points. Then,

spatial unmixedness within each new grid is calculated based on these 25 data points. Results within

the black solid line (in Fig. 10 Plane c) are plotted in Fig. 12; it can be seen that the region where

spatial unmixedness is large and the region where isolines of mixture fraction are dense has a

substantial degree of overlap. Based on this fact, it can be inferred that the region with poor mixing favors the region where mixture fraction gradient is large. It might be possible to use the gradient of mixture fraction to roughly indicate the degree of unmixedness. Much less samples are needed to plot f isolines than to calculate U_s after all. How big the degree of this overlap is remains to be further explored.
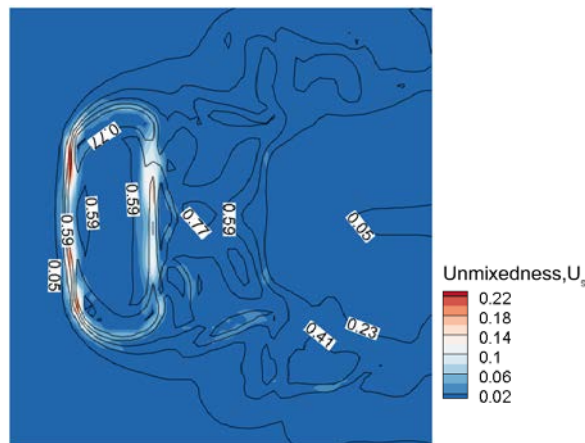

Figure 12. The distribution of spatial unmixedness U_s in a selected area in Plane c (in Fig. 10). Plane c locates at a height of $y/d = 3.79$, the area is shown as a black square. Black lines in Fig. 12 mark the isolines of mixture fraction f. The data is based on the spatial distribution of the components at $t = 2\tau$, each grid cell contains 25 samples.

In order to investigate further the relationship between unmixedness and mixture fraction, U_s and f in plane c are shown in a scatter plot (Fig. 13). It can be observed that most of the data points are concentrated in the region $U_s \leq 0.02$, corresponding to the deep blue region in Fig. 12, i.e., the region where the mixture fraction is almost uniform.
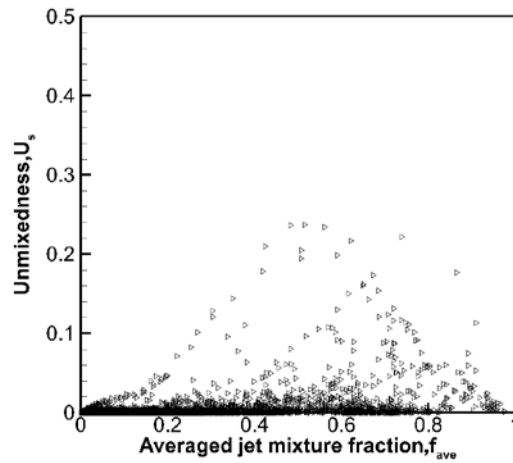
Figure 13. Scatter plot of spatial unmixedness U_s and average mixture fraction f_{ave} in plane c. Plane c locates at a height of $y/d = 3.79$. The data is based on the spatial distribution of the components at $t = 2\tau$, each grid cell contains 25 samples.

In the three-dimensional space, the computational domain is re-divided into a $180 \times 120 \times 120$ mesh. Since the original mesh is $900 \times 600 \times 600$, each new grid cell contains 125 data points. Spatial unmixedness of each new grid is calculated based on those 125 samples within it. Distribution of U_s in 3D space is shown in Fig. 14. The isosurface of the mixture fraction is used to illustrate the shape of the JICF. Results show a poorly mixed area on the windward side, while the goodness of mixing rapidly increases as the jet penetrates into the crossflow. This is the evidence that most of the mixing process takes place in the vicinity of the jet outlet. Under the same mixture fraction, there is also an area with high unmixedness on the leeward side of the jet, whereas the shear vortex on both sides of the jet has a better mixing condition.
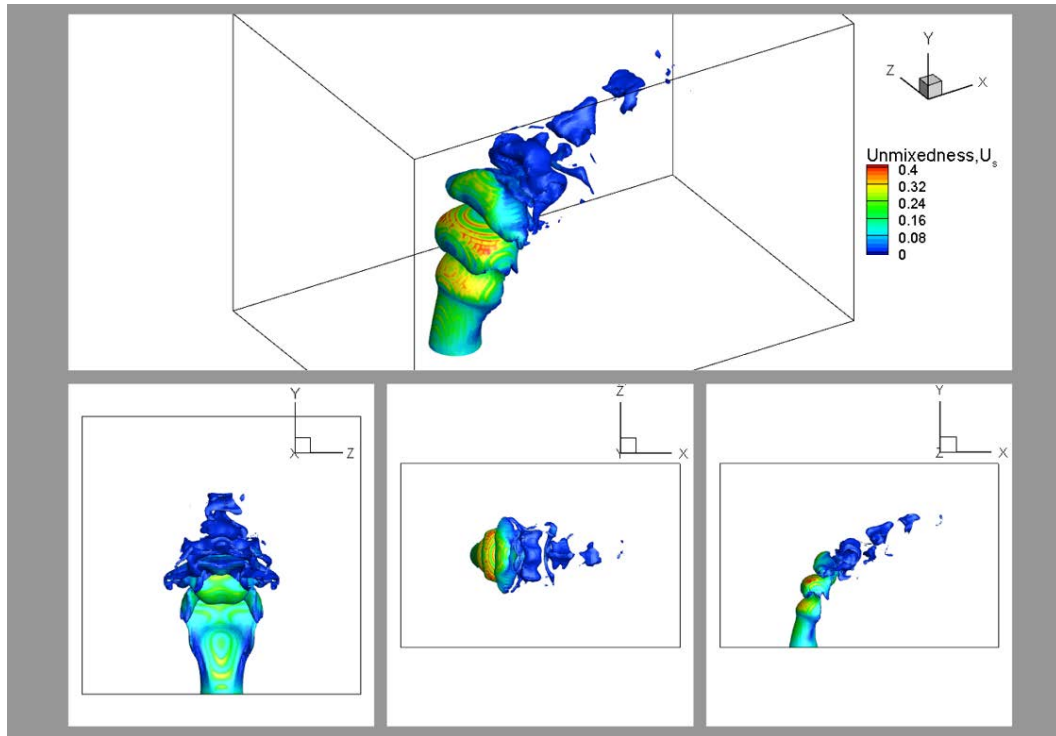
Figure 14. Mixing of jet in crossflow in three-dimensional space. Isosurface of mixture fraction $f_{ave} = 0.5$ shows the shape of the jet. Color on the isosurface shows spatial unmixedness U_s. The data is based on the spatial distribution of the components at $t = 2\tau$, and each grid cell contains 125 samples.

In the scatter plot of U_s and f_{ave}, most of the points concentrate on the lower side, as shown in Fig. 15. This corresponds to the area of pure crossflow and pure jet in space. In order to better demonstrate the distribution relationships between U_s and f_{ave}, the points of $U_s < 0.04$ are eliminated when the joint probability distribution function is plotted. Figure 16 gives a wealth of information, including the probability distribution of U_s at any f_{ave}. The widest distribution of U_s appears near $f_{ave} = 0.6$, which means the poorest mixing condition appears when mixture fraction is around 0.6.
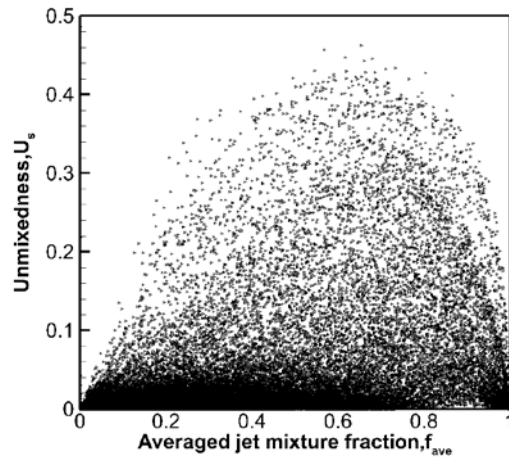
Figure 15. Scatter plot of spatial unmixedness U_s and average mixture fraction f_{ave} in three-dimensional space. The data is based on the spatial distribution of the components at $t = 2\tau$; each grid cell contains 125 samples.
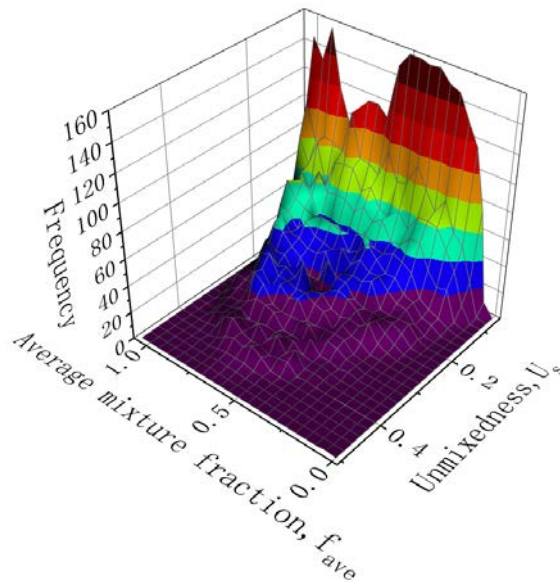

Figure 16. Joint probability distribution function of U_s and f_{ave}. $0.04 \leq U_s \leq 0.5$, and is divided into 23 intervals. $-0.05 \leq f_{ave} \leq 1.05$, and is divided into 22 intervals.

The isosurface of $U_s = 0.01$ exhibits a two-layer structure, so it needs to be displayed with a transparent isosurface, as shown in Fig. 17. The color shows the average mixture fraction. The space between the two layers is the region where U_s increases and then decreases. In other words, mixing condition changes from good to bad and then to good again between these two layers. It is worth noting that the value of f_{ave} is very different in these two layers; this observation again confirms the conclusion in Fig.10. The region with large spatial unmixedness U_s and the region with large f_{ave} gradient have a substantial degree of coincidence. Further, most of the space sandwiched by the two layers is concentrated near the jet exit, and a small portion exists downstream of the jet trajectory, dispersedly. The region surrounded by the isosurface denotes the region where most of the mixing process takes place. Results show that mixing between the jet and crossflow takes place as soon as the jet is injected. Most of the mixing zone surrounds the jet, and breaks rapidly as the jet shear vortex breaks.
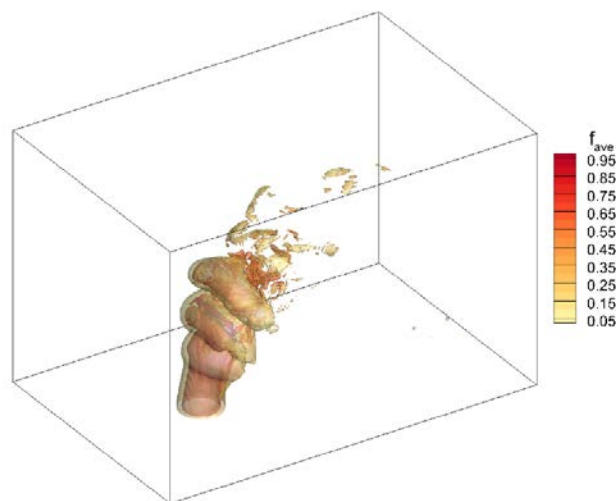
Figure 17. Mixing of jet in crossflow in three-dimensional space. Transparent surface is the isosurface of spatial unmixedness $U_S = 0.01$. Color on the isosurface shows the average mixture fraction f_{ave}. The data is based on the spatial distribution of the components at $t = 2\tau$, and each grid cell contains 125 samples.

3.3.3 Effects of jet-to-crossflow momentum flux ratio on mixing.

In order to show the influence of the jet-to-crossflow momentum flux ratio on mixing between the fuel jet and the oxygen-rich crossflow, simulation data of Case 1 ($J = 9$) and Case 2 ($J = 0.8$) are compared. 3D isosurfaces of unmixedness U_S from the two cases are shown in Fig. 18. The same U_S value ($U_S = 0.0005$) has been retained for both plots in order to facilitate comparison. In each case, the isosurface shows a double-layer structure (with a windward and leeward side), and the enclosed volume can be used to represent the location where the fluids have been sufficiently mixed. This enclosed volume is referred to as mixing zone in the following paragraph. When checking the influence of a particular value for U_S on the shape of the isosurfaces, it is found that a smaller U_S will make the space between the two isosurfaces larger, as expected, while delivering similar shapes as long as the same range is considered. This trend can be observed by comparing the left image (for $J = 9$) in Fig. 18 with Fig. 17; the isosurface of $U_S = 0.0005$ encloses a larger volume. In the current analysis, the mixing goodness corresponding to $U_S = 0.0005$ has been selected as a suitable marker of the well-mixed zone.
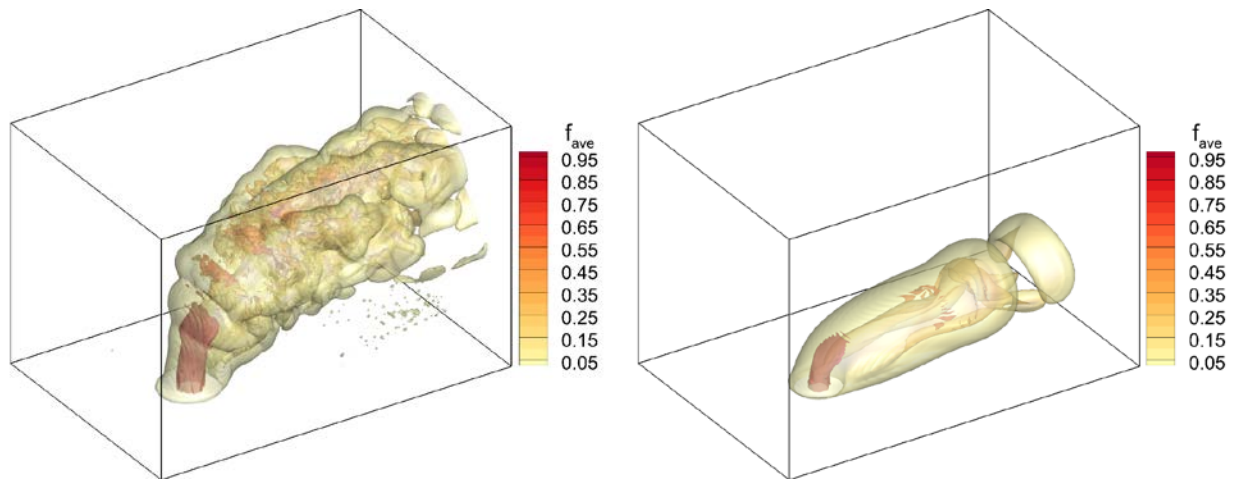
Figure 18. Mixing quality of the $J = 9$ case (left) and $J = 0.8$ case (right). The transparent surface plotted here is the isosurface of spatial unmixedness $U_s = 0.0005$. Color on the isosurface shows the average mixture fraction f_{ave}.

Comparing now Fig.18 and Fig.3, it can be seen that the shape of the mixing zone is somewhat similar to the shape of the jet vortex structures, but smoother. For both values of J, it is observed that the outer isosurface $U_s = 0.0005$ wraps around the main jet vortex structures. The main difference is that, in the $J = 9$ case, the resulting vortex structures are far more complicated, so that the U_s isosurface is more folded. This is particularly visible in the jet shear region and near to the area where the vortex rings are broken. By comparison, the U_s isosurface of the $J = 0.8$ case is much smoother. In summary, the vortex structures resulting from the JICF configuration show features similar to the mixing zone; both are far more complex and contorted in the $J = 9$ case compared to $J = 0.8$.
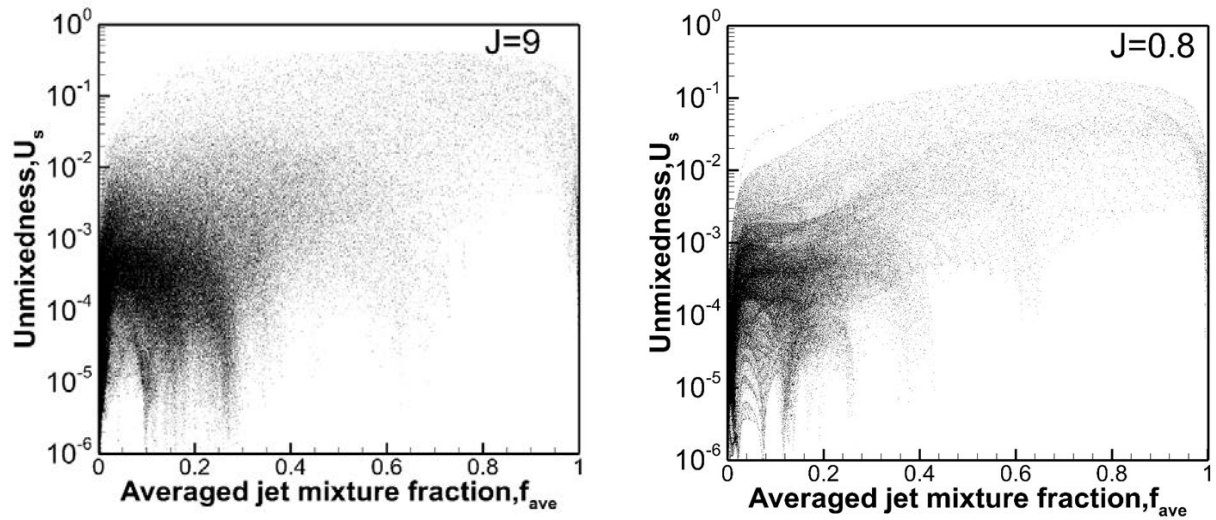
Figure 19. Scatter plot of spatial unmixedness U_s and average mixture fraction f_{ave} in three-dimensional space. Note the logarithmic vertical scale, identical for both plots.

In order to quantitatively compare the goodness of mixing in the two cases, the distribution of spatial unmixedness U_s versus average mixture fraction f_{ave} is plotted in Fig. 19. The same logarithmic coordinate is used in the two plots to enable a direct comparison. Somewhat surprisingly, these results show that the $J = 0.8$ case is somewhat better mixed than the $J = 9$ case. One reason possibly explaining this behavior is the very high molecular diffusion of hydrogen. It must be kept in mind that the jet velocity in Case 2 ($J = 0.8$) is only about one-fifth of the jet velocity in Case 1. In other words, in Case 2, the residence time of the fuel jet in the computational domain is more than four times longer than in Case 1. This longer residence time combined with the very high diffusion velocity of hydrogen leads to a higher contribution of molecular diffusion, so that the mixture is slightly more uniform in spite of weaker vortical structures. For the JICF

configuration, the mixing is controlled by both entrainment rate and molecular diffusion. While turbulent entrainment dominates Case 1, it appears that molecular diffusion plays an important role in Case 2.
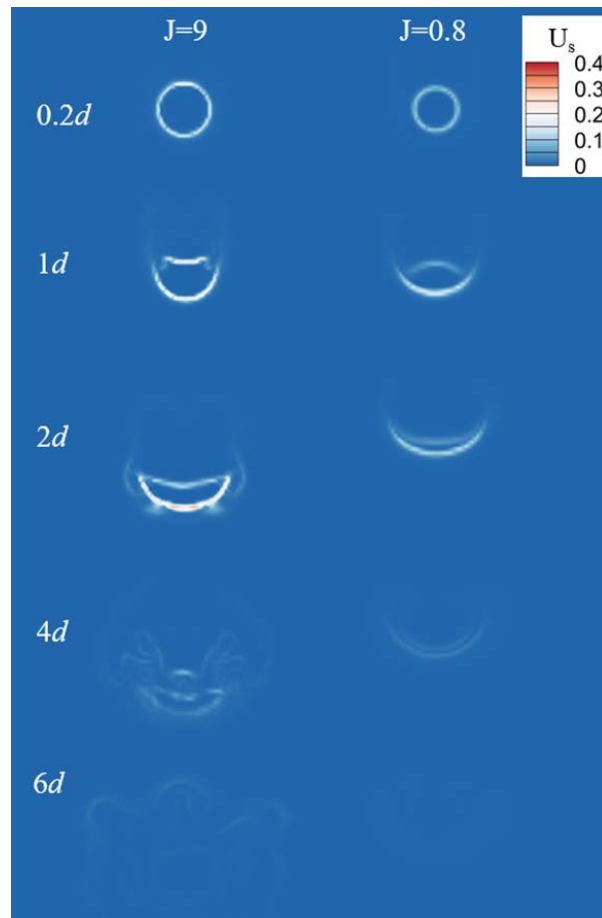

Figure 20. Spatial unmixedness U_s shown along different slices perpendicular to the jet trajectory. The distance between center of jet exit and the intersections of jet trajectory and the slices ranges from 0.2d to 6d (0.2d, 1d, 2d, 4d, 6d).

As pointed out by previous studies[1,2], a larger jet-to-crossflow momentum flux ratio can accelerate the mixing process of the jet and the crossflow. Though it might first appear to go in the other way, Figure 20 indeed confirms this conclusion. All the cross-sections shown in Fig. 20 are perpendicular to the jet trajectory, at increasing distance from the jet exit plane ($0.2d$, $1d$, $2d$, $4d$, and $6d$, respectively). For a proper comparison, it must once again be kept in mind that the jet velocity in Case 2 ($J = 0.8$, right part of Fig. 20) is only about one-fifth of the jet velocity in Case 1 (left part of Fig. 20). Taking this jet velocity as constant along the trajectory – which is obviously a poor approximation, but sufficient for a first qualitative analysis, an element from the fuel jet in Case 2 ($J = 0.8$) would arrive at the level of section 1d at about the same time that an element from the fuel jet in Case 1 would leave section 4d. This means that, for a fair comparison, the second image of the right column must be compared to the fourth one of the left column. Obviously, at the same time, the case $J = 9$ leads locally to a more uniform mixing status, compared to the $J = 0.8$ case. This also explains the difference between Figure 19 and Figure 20; while Figure 20 looks at specific positions in space – and, connected to a convective velocity, in time –, Figure 19 shows an instantaneous image of the whole domain, without any details in time and space. Both views are important and complementary, revealing different features of the process.

4 Conclusions

A reacting hydrogen jet in a transverse vitiated crossflow was investigated using DNS. The reactive Navier-Stokes equations, coupled with transport equations for multispecies diffusion and chemical reactions, were solved in the low-Mach regime with high-order, numerically efficient algorithms. To account for the strong thermo-diffusion effect of hydrogen combustion, the Soret term was included in the simulations. The flow field and flame structure were depicted along the jet trajectory. The heat release rate and chemical explosive mode analysis were employed to identify the combustion mode. Mixing characteristics of the reacting JICF were studied in detail. The main results can be summarized as follows:

• Along the jet trajectory, the cross-section of flame/fuel/velocity transitions from a circle to an ellipse and then to a kidney-like shape. Further downstream, structures are dominated by a counter-rotating vortex pair.

• The flame is anchored around the jet exit, and downstream combustion happens only on the windward side. The highest temperature locates in the recirculation zone on the jet lee side.

• Diffusion flame is the predominant combustion mode, though some premixed flames or partially premixed flames are found at the windward shear layer.

• Scale of segregation as well as spatial unmixedness is used as a quantification of mixing characteristic in the jet direction. Spatial unmixedness is calculated in smaller 2D regions and 3D space taking advantage of more data points. Results show detailed information of spatial mixing.

• In three-dimensional space, there is a substantial degree of overlap between the region with high spatial unmixedness and the region with high mixture fraction gradient.

• The jet vortex structure and the shape of the mixing zone show similar structures, with a more complex topology and stronger folding for the $J = 9$ case compared to the $J = 0.8$ case. The mixing process is faster in time for the $J = 9$ case, while there is a much longer residence time for mixing in the $J = 0.8$ case, in connection with a very high diffusion velocity of hydrogen.

The above findings have implications for the design and operation of combustors using the reacting JICF configuration. The prime example is gas turbines with multi-stage fuel/air injections with aim to achieving high efficiency and low emissions. Improved understanding about the jet and cross flow interactions, mixing and combustion modes as reported in this paper is crucial to avoid combustion instability and/or incomplete combustion. Finally, the low-Mach-number based multicomponent reactive flow DNS method implemented in DINO is shown to be capable of reproducing the key DNS results of Lyra et al. [9] using a full compressible formulation. With the high computational efficiency and capability to handle complex geometries, DINO has the potential to explore more realistic reactive JICF phenomena and even combustion in engine configurations in follow-on work.

Acknowledgment

References

1.   Mahesh, K. The Interaction of Jets with Crossflow. In *Annual Review of Fluid Mechanics, Vol 45*, Davis, S. H.; Moin, P. Eds. Annual Reviews: Palo Alto, **2013**; Vol. 45, 379-407.

2.   Karagozian, A. R. Transverse jets and their control. *Progress in Energy and Combustion Science* **2010,** 36, (5), 531-553.

3.   Johari, H. Scaling of fully pulsed jets in crossflow. *AIAA Journal* **2006,** 44, (11), 2719-2725.

4.   Pratte, B. D.; Baines, W. D. Profiles of the round turbulent jet in a cross flow. *Journal of the Hydraulics Division* **1967,** 93, (6), 53-64.

5.   Weinzierl, J.; Kolb, M.; Ahrens, D.; Hirsch, C.; Sattelmayer, T. Large-Eddy Simulation of a Reacting Jet in Cross Flow With NOx Prediction. *Journal of Engineering for Gas Turbines and Power* **2017,** 139, (3), 7.

6.   Pinchak, M. D.; Shaw, V. G.; Gutmark, E. J. The effects of nozzle geometry and equivalence ratio on a premixed reacting jet in vitiated cross-flow. *Combustion and Flame* **2018,** 191, 353-367.
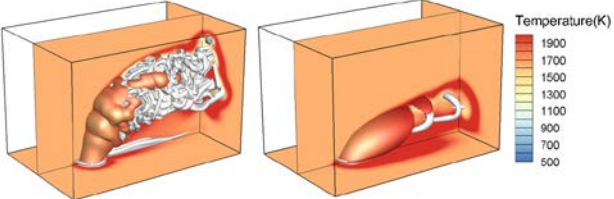
7.   Wagner, J. A.; Grib, S. W.; Renfro, M. W.; Cetegen, B. M. Flowfield measurements and flame stabilization of a premixed reacting jet in vitiated crossflow. *Combustion and Flame* **2015,** 162, (10), 3711-3727.

8.   Grout, R. W.; Gruber, A.; Yoo, C. S.; Chen, J. H. Direct numerical simulation of flame stabilization downstream of a transverse fuel jet in cross-flow. *Proceedings of the Combustion Institute* **2011,** 33, (1), 1629-1637.

9.   Lyra, S.; Wilde, B.; Kolla, H.; Seitzman, J. M.; Lieuwen, T. C.; Chen, J. H. Structure of hydrogen-rich transverse jets in a vitiated turbulent flow. *Combustion and Flame* **2015,** 162, (4), 1234-1248.

10.   Abdilghanie, A.; Frouzakis, C. E.; Fischer, P. Direct numerical simulation of autoiginition of a hydrogen jet in a preheated cross flow. Paper #070LT-0251, 8thUS National Combustion Meeting, The University of Utah, May 19-22, **2013**.

11.   Leong, M. Y.; S. Samuelsen, G.; Holdeman, J. Optimization of Jet Mixing Into a Rich, Reacting Crossflow. *Journal of Propulsion and Power* **1998**, 16, (5), 739-735.

12.   Leong, M. Y.; Samuelsen, G. S.; Holdeman, J. D. Mixing of jet air with a fuel-rich, reacting crossflow. *Journal of Propulsion and Power* **1999,** 15, (5), 617-622.

13.   Demayo, T. N.; Leong, M. Y.; Samuelsen, G. S.; Holdeman, J. D. Assessing jet-induced spatial mixing in a rich, reacting crossflow.   *Journal of Propulsion and Power* **2013,** 19, (1), 14-21.

14.   Minamoto, Y.; Kolla, H.; Grout, R. W.; Gruber, A.; Chen, J. H. Effect of fuel composition and differential diffusion on flame stabilization in reacting syngas jets in turbulent cross-flow. *Combustion and Flame* **2015,** 162, (10), 3569-3579.

15.   Kolla, H.; Grout, R. W.; Gruber, A.; Chen, J. H. Mechanisms of flame stabilization and blowout in a reacting turbulent hydrogen jet in cross-flow. *Combustion and Flame* **2012,** 159, (8), 2755-2766.

16.   Grout, R. W.; Gruber, A.; Kolla, H.; P.-T, B.; Bennett, J. C.; Gyulassy, A.; Chen, J. H. A direct numerical simulation study of turbulence and flame structure in transverse jets analysed in jet-trajectory based coordinates. *Journal of Fluid Mechanics* **2012,** 706, 351-383.

17.   de Charentenay, J.; Thévenin, D.; Zamuner, B. Comparison of direct numerical simulations of turbulent flames using compressible or low-Mach number formulations. *International Journal for Numerical Methods in Fluids* **2002,** 39, (6), 497-515.

18.   Abdelsamie, A.; Fru, G.; Oster, T.; Dietzsch, F.; Janiga, G.; Thévenin, D. Towards direct numerical simulations of low-Mach number turbulent reacting and two-phase flows using immersed boundaries. *Computers & Fluids* **2016,** 131, 123-141.

19.   Majda, A.; Sethian, J. The Derivation and Numerical Solution of the Equations for Zero Mach Number Combustion. *Combustion Since and Technology* **1985**, 42,(3-4), 185-205.

20.   Giovangigli, V. Multi-Component Flow Modeling, Birkhäuser: Boston, **1999**, 6-46.

21.   Chi, C.; Abdelsamie, A.; Thévenin, D. Direct Numerical Simulations of Hotspot-induced Ignition in Homogeneous Hydrogen-air Pre-mixtures and Ignition Spot Tracking. *Flow Turbulence and Combustion* **2018,** 101, (1), 103-121.

22.   Chi, C.; Janiga, G.; Abdelsamie, A.; Zaehringer, K.; Turanyi, T.; Thévenin, D. DNS Study of the Optimal Chemical Markers for Heat Release in Syngas Flames. *Flow Turbulence and Combustion* **2017,** 98, (4), 1117-1132.

23.   Goodwin, D. G.; Speth, R. L.; Moffat, H. K.; Weber, B. W. Cantera: An object-oriented software toolkit for chemical kinetics, thermodynamics, and transport processes. https://www.cantera.org.

24.   Li, J.; Zhao, Z.; Kazakov, A.; Dryer, F. L. An updated comprehensive kinetic model of hydrogen combustion. *International Journal of Chemical Kinetics* **2010,** 36, (10), 566–575.

25.   Hilbert, R.; Tap, F.; El-Rabii, H.; Thévenin, D. Impact of detailed chemistry and transport models on turbulent combustion simulations. *Progress in Energy and Combustion Science* **2004**, 30, (1), 61-117.

26.   Hirschfelder, J.; Curtiss, C.; Bird, R. Molecular theory of gases and liquids. Wiley: New York, **1954**, 511-512.

27.   F. Hussain. Coherent structures: reality and myth. *Physics of Fluids* **1983**, 26, 2816-2850.

28.   Bremer, P. T.; Gruber, A.; Bennett, J.; Gyulassy, A.; Kolla，H.; Chen, J.; Grout, R. Identifying turbulent structures through topological segmentation. Communications in Applied Mathematics and Computational Science, **2015**. 11(1): p. 37-53.

29.   Nair, V.; Sirignano, M.; Schmidheiser, S.; Dillon, L.; Fugger, C. A.; Tongxun, Y.; Naibo, J.; Hsu, P.; Slipchenko, M. N.; Roy, S.; Emerson, B.; Steinberg, A.; Lieuwen, T. C. Tomographic PIV characterization of the near field topology of the reacting jet in crossflow. *AIAA Scitech 2020 Forum.* **2020**.

30.   Muppidi, S.; Mahesh, K. Direct numerical simulation of passive scalar transport in transverse jets. *Journal of Fluid Mechanics* **2008,** 598, 335-360.

31.   Muppidi, S.; Mahesh, K. Direct numerical simulation of round turbulent jets in crossflow. *Journal of Fluid Mechanics* **2007,** 574, 59-84.

32.   Lu, T. F.; Yoo, C. S.; Chen, J. H.; Law, C. K. Three-dimensional direct numerical simulation of a turbulent lifted hydrogen jet flame in heated coflow: A chemical explosive mode analysis. *Journal of Fluid Mechanics* **2010,** 652, (4), 45-64.

33.   Messig, D.; Vascellari, M.; Hasse, C. Flame structure analysis and flamelet progress variable modelling of strained coal flames. *Combustion Theory & Modelling* **2017,** 21, (4), 1-22.

34 Cortesi, A. B.; Smith, B. L.; Yadigaroglu, G.; Banerjee, S., Numerical investigation of the entrainment and mixing processes in neutral and stably-stratified mixing layers. *Physics of Fluids* **1999**, 11, (1), 162-185.

35.   Dimotakis, P. E. The mixing transition in turbulent flows. *Journal of Fluid Mechanics* **2000**, 409, (01), 69-98.

36.   Shan, J. W.; Dimotakis, P. E. Reynolds-number effects and anisotropy in transverse-jet mixing. *Journal of Fluid Mechanics* **2006**, 566.

37.   Danckwerts, P. V. The definition and measurement of some characteristics of mixtures. *Applied Scientific Research* **1952,** 3, (4), 279-296.

38.   Liscinsky, D., True, B., Holdeman, J. Experimental investigation of crossflow jet mixing in a rectangular duct. *NASA Technical Memorandum 106152 AIAA-93-2037*. **1993**. DOI: 10.2514/6.1993-2037

TOC Graphic